

# Lifetime Prediction of Ceramic Components – A Case Study on Hybrid Rolling Contact

Iyas Khader<sup>1,2</sup>, Stefan Rasche<sup>3</sup>, Tanja Lube<sup>3</sup>, Rahul Raga<sup>2</sup>, Ulrich Degenhardt<sup>4</sup>, Andreas, Kailer<sup>2</sup>

<sup>1</sup>Department of Industrial Engineering, German-Jordanian University, P.O. Box 35247, Amman 11180, Jordan

<sup>2</sup>Fraunhofer-Institute for Mechanics of Materials IWM, Wöhlerstraße 11, 79108 Freiburg, Germany

<sup>3</sup>Institut für Struktur- und Funktionskeramik der Montanuniversität Leoben, Peter-Tunner-Strasse 5, 8700 Leoben, Austria

<sup>4</sup>FCT Ingenieurkeramik GmbH, Gewerbepark 11, 96528 Frankenblick, Germany

## Abstract

In this study, fatigue life predictions were made for silicon nitride components undergoing hybrid ceramic-steel rolling contact. Three-dimensional stress fields were extracted using a bespoke finite element model and subsequently used to calculate stress intensity factors by means of the weight function method. Crack-growth rates were estimated by assuming crack growth to follow a Paris power-law expression whose material parameters were obtained from four-point bending fatigue experiments under fluctuating tensile load ( $R = 0.1$ ) and fully-reversed alternating load ( $R = -1$ ).

The crack-growth behavior obtained from the calculations was compared with experimental results obtained from twin-disk-type RCF experiments. The calculated lifetime predictions were in accordance with the experimental results. Crack formation and propagation was found more likely to occur in locations undergoing alternating load rather than those undergoing pure fluctuating tensile load.

### *Keywords:*

Silicon nitride, rolling-contact fatigue, stress intensity factor, weight function method, lifetime prediction, negative load ratio.

## 1 Introduction

Ceramic rolling elements made of silicon nitride possess exceptional advantages over conventional

steel bearings in terms of hardness, chemical stability, long life, and low density. Additionally, the low adhesion affinity between steel and silicon nitride [1, 2] provides significant advantage for hybrid bearings in marginal lubrication conditions.

Rolling elements such as bearing balls undergo one of the most severe mechanical loading of all machine elements. The stresses engendered in application are extremely localized and bound to a very small volume of the loaded material – both on the surface and in the depth. A plethora of literature is available on the topic of rolling-contact fatigue (RCF) of silicon nitride [3, 4, 5, 6]; for recent reviews cf. [5, 7, 8]. On the macroscopic scale, RCF is regarded as cyclic crack growth, which is governed by a complex three-dimensional time-dependent contact stress field.

There is a general agreement that fatigue cracks in ceramics, except for phase-transforming ceramics, are associated with pre-existing flaws [9, 10]. Therefore, fatigue life predictions of ceramic components can be contemplated by assuming that macroscopic cracks develop from pre-existing flaws. Moreover, there are no known differences to exist between static and cyclic loading conditions as far as the mechanisms of microscopic deformation or microcrack nucleation are concerned [11]. It has been shown that the mechanism of crack advancement in ceramics is identical under cyclic and static loading, whereas, in the former crack shielding in the crack wake is constantly weakened by cyclic loading, particularly during unloading [9]. For instance, by considering frictional grain bridging to be the predominant shielding mechanism in silicon nitride, Dauskardt [12] developed a conceptual model, based on cyclic sliding wear, to explain its degradation. It was argued that repetitive sliding wear eventually leads to a decrease in the toughening capacity of the bridging zone by reducing the frictional pullout stress, hence, reduces grain bridging stress and exposes the crack tip to an increased portion of the applied stress intensity. A recent review of fatigue degradation in ceramics, which summarizes the described mechanisms, can be found in Ritchie and Launey [13].

Studies have shown that crack-growth rate in engineering ceramics under cyclic load is primarily dependent on the maximum stress intensity  $K_{max}$  rather than the stress intensity range  $\Delta K$  [14, 15, 16, 17]. The strong  $K_{max}$  dependence is often explained in the light of the primary crack-advancing mech-

anism, which is identical in cyclic loading to that under static loading; whereas, the weak  $\Delta K$  dependence is attributed to a mere effect of shield degradation primarily occurring during unloading; a treatment of this topic pertaining to silicon nitride ceramics can be found in [18, 19].

The work of Lube et al. [20] enabled the identification of distinct differences on the microscopic level in the failure mechanism of silicon nitride subjected to fluctuating tensile load ( $R = 0.1$ ) and alternating “fully-reversed” load ( $R = -1$ ); the latter is similar to the loading scenario prevailing in rolling contact.

Prediction of crack growth and lifetime in ceramic components can be foreseen by calculating stress intensity factor (SIF) cycles for cracks at various locations. Fatigue life estimation is expressed as the number of load cycles a crack experiences until a certain crack length has been reached or until critical crack growth is predicted; hence, a Paris power-law [21] can describe the phenomenon of cyclic crack growth. Numerical methods, such as the finite element method (FEM), can be used to solve fracture mechanics problems through incorporating incremental crack-growth laws. Nevertheless, they are very expensive in terms of time and computational resources; thus, become impractical in conducting systematic studies for different contact geometries and crack paths. The calculation of time-dependent SIFs for a surface crack of several positions, orientations, and sizes can be accomplished through a much simplified approach [22, 23] relying on the weight function procedure developed by Bückner [24] and Rice [25]. This approach merely requires the knowledge of the crack path geometry, the stresses within and normal to the crack plane (plane cracks are assumed for simplification), and an approximate weight function suitable to the crack geometry.

In the work of Lengauer and Danzer [26], the weight function method was applied to calculate SIFs and subsequently to estimate lifetimes of silicon nitride rolls applied in rolling wire. The SIF calculations were based on stress fields obtained from finite element (FE) simulations. The authors explained the pop-in crack-growth behavior that occurs in the ceramic rolls, wherein, the stress intensity during contact with the wire exceeds the fracture toughness of the material. Hence, lifetime estimation was mainly concerned with overloaded work-rolls.

The present work aims at developing a method to estimate fatigue life in ceramic components undergoing rolling contact. It combines experimental and numerical work on RCF failure in hybrid ceramic-steel contact. The stress distribution for a twin-disk test configuration was calculated using the implicit solver of ABAQUS for three-dimensional cases of fully-elastic and elastoplastic material behavior and then exported along with the nodal data into a bespoke code programmed in Python to determine the stress intensity factors based on the weight-function method. Subsequently, crack-growth rates in the ceramic were estimated by relying on material parameters obtained experimentally from cyclic bending fatigue tests carried at two distinct load ratios. The challenge associated with this work lies in synthesizing experimental methods with computationally inexpensive numerical schemes to yield an experimentally validated accurate estimation of ceramic component lifetimes.

## 2 Experimental

All experiments were performed on a commercial silicon nitride (grade SN-GP black, FCT – Ingenieurkeramik GmbH, Frankenblick, Germany). The material was fully characterized by a multitude of experiments in [27].

### 2.1 Four-point bending fatigue tests

Four-point bending strength [28], fracture toughness [29] and four-point bending cyclic fatigue tests were carried out to obtain relevant material properties [20, 30, 27]. The room temperature fracture toughness of SN-GP black was found to be  $K_{IC,air}=5.62\pm 0.09$  MPa·m<sup>1/2</sup> and  $K_{IC,water}=5.39\pm 0.07$  MPa·m<sup>1/2</sup> in air and in water, respectively [27].

The fatigue tests were performed under various conditions at a frequency of  $f=40$  Hz with a cut-off at  $10^7$  cycles. Fluctuating tensile loading (tension-tension) tests at a load ratio of  $R = 0.1$  were carried out under water and in lab air and alternating (tension-compression) tests at a load ratio of  $R = -1$  were carried out in lab air. Only at the lowest stress levels, some survivals were observed. The tests were evaluated by following the procedure described by Munz and Fett [31] in order to obtain  $da/dN$  versus  $K_{I,max}$  curves.

## 2.2 Rolling-Contact Experiment

RCF experiments were carried out on a twin-disk tribometer under continuous oil lubrication (non-additivated mineral oil SKF TT9, Kroon Oil BV, The Netherlands), Fig. 1(a). A cylindrical silicon nitride (grade SN-GP black, FCT – Ingenieurkeramik GmbH, Frankenblick, Germany) rollers with outer diameter of 60 mm was brought into rolling contact with a crowned hardened 100Cr6 (AISI 52100) steel disk (HRC 64) with outer diameter of 60 mm and a crown radius of 5 mm, see Fig. 1(b).

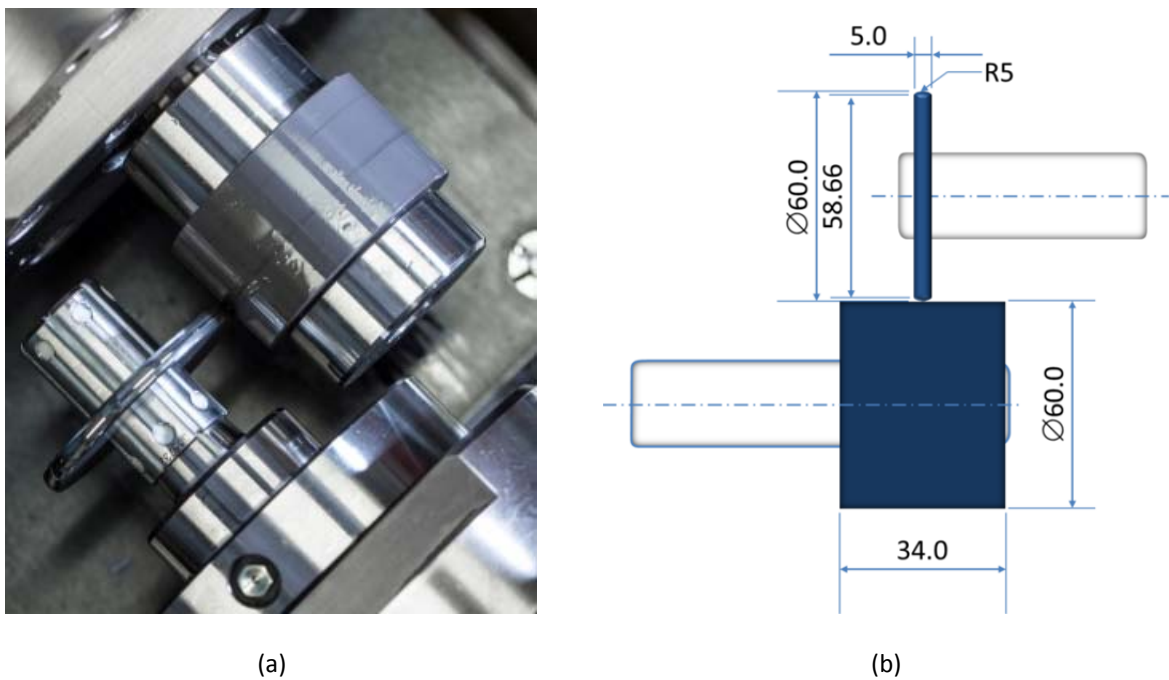


Fig. 1. (a) Twin-disk tribometer, (b) schematic diagram of the rolling-contact test setup showing the dimensions of the samples

SN-GP black is a gas-pressure sintered silicon nitride (GPSN). Its microstructure contains  $\beta$ - $\text{Si}_3\text{N}_4$  grains and ca. 10 wt.% secondary glassy phase of the sintering additives  $\text{Y}_2\text{O}_3$  and  $\text{Al}_2\text{O}_3$ .

The disk and roller were both rotated at 1500 rpm (i.e., without induced slip). A normal force ( $F_N$ ) was applied to the samples in contact. Throughout the experiments, the tribometer measured and recorded the torque generated in contact, from which the coefficient of friction (COF) is calculated. A summary of the experimental parameters is listed in Table 1.

The experiments were stopped after specific intervals to inspect the surfaces of the ceramic samples.

Table 1. Parameters of the RCF experiments and simulations

Material pairing	SN-GP black / 100Cr6
Applied normal load $F_N$ [N]	500, 850, 2500, and 4150
Rotational velocity of the ceramic roller / steel disk [rpm]	1500 / 1500
Slip ratio	0.0
Diameter of ceramic roller / steel disk [mm]	60 / 60
Crown radius of steel disk [mm]	5
Lubricant	SKF TT9 Density at 20 °C: 0.876 g/cm <sup>3</sup> Kinematic viscosity at 40 °C: 8.81 mm <sup>2</sup> /s

### 3 Finite element simulations

The contact stresses engendered in rolling contact were calculated for the twin-disk test configuration described above using a quasi-static three-dimensional FE simulation in ABAQUS/Standard. Due to the symmetry of the system, only one half of the geometry was modeled. The model was comprised of a crowned disk with a circular profile rolling on the surface of a flat roller with a predefined normal force. Pure rolling with no gross slip was set between contacting surfaces by fixing the rotational velocities of both contacting partners. Modeling the rolling contact was accomplished by initially applying a Lagrangian approach to initialize contact (progressive compression of the two bodies). Rigid body rotations were subsequently described using a moving reference frame, wherein an Eulerian approach was adopted, by which the material is transported through the mesh. Details related to this modeling technique can be found elsewhere [32].

In a first set of simulations, both silicon nitride and 100Cr6 steel were modeled as linear elastic materials with the room-temperature elastic properties listed in Table 2. To account for plastic deformation in the steel disk, a second set of simulations was constructed with steel modeled with elastoplastic behavior. A rate-independent isotropic material model was adopted for metal plasticity. The uniaxial yield strength of 100Cr6 was set to 1100 MPa and strain hardening was incorporated using tabular experimental stress-strain data obtained from [33].

Table 2. Room-temperature elastic properties of the contact partners

<b>Material</b>	<b>Elastic modulus [GPa]</b>	<b>Poisson's ratio [-]</b>
Silicon nitride "SN-GP black"	293	0.26
100Cr6 steel	212	0.29

The three-dimensional geometry was discretized using standard hexahedral C3D8 elements in ABAQUS. Coulomb friction with a load-dependent coefficient of friction was assumed to model friction. The coefficient of friction was experimentally determined for each applied load from the tribometer data.

### 3.1 Mesh refinement parametric study

The development of a full three-dimensional model to simulate the rolling-contact problem was preceded by following a parametric approach to choose a mesh that accurately captures the maximum tensile stresses (i.e., the stresses that are responsible for crack advancement/propagation in ceramics). The mesh was optimized with particular refinement in the vicinity of the contact zone as listed in Table 3.

Table 3. Summary of smallest element size in the contact zone for different mesh densities; diagonally hatched fields indicate an increase in element size, shaded fields indicate a reduction in element size, and clear fields indicate no change in element size

<b>Direction</b>	<b>Minimum element length in the specified direction [<math>\mu\text{m}</math>]</b>			
	<i>Mesh01</i> (reference)	<i>Mesh02</i>	<i>Mesh03</i>	<i>Mesh04</i>
Radial ( $\rho$ )	50	22.5	4.5	4.5
Circumferential ( $\Phi$ )	50	87	44	20
Axial ( $Z$ )	50	55	22.5	22.5
Total number of degrees of freedom ( $\text{DOF} \times 10^6$ )	2.04	0.47	1.00	1.18

The area resulting from the contact of the two bodies is elliptical in shape, having semi-axes  $r_1$  and  $r_2$ . A semi-analytical solution is readily available in [34] for the calculation of the maximum principal stress (tensile stress) at the major and minor radii of the contact ellipse ( $r_1$  and  $r_2$ ) using the expressions

$$\sigma_{r_1} = p_o(1 - 2\nu) \frac{r_2}{r_1 \epsilon^2} \left( \frac{1}{\epsilon} \tanh^{-1} \epsilon - 1 \right) \quad (1)$$

$$\sigma_{r_2} = p_o(1 - 2\nu) \frac{r_2}{r_1 \epsilon^2} \left( 1 - \frac{r_2}{r_1 \epsilon} \tan^{-1} \left( \frac{r_1 \epsilon}{r_2} \right) \right) \quad (2)$$

where  $\nu$  is Poisson's ratio,  $p_o$  the maximum contact pressure at the center of the contact ellipse, which is given for an applied normal load  $F_N$  by the expression

$$p_o = \frac{3F_N}{2\pi r_1 r_2} \quad (3)$$

and  $\epsilon$  the eccentricity of the ellipse, which can be expressed as follows

$$\epsilon = \left[ 1 - \left( \frac{r_2}{r_1} \right)^2 \right]^{1/2}, \quad r_2 < r_1 \quad (4)$$

The tensile stresses developed at the major and minor contact radii, Eqs. (1) and (2), become increasingly different than that of a circular contact and from one another as the contact becomes "more elliptical" (i.e., the major radius becomes increasingly larger than the minor radius). The Hertzian contact solution results in a higher tensile stress at the major contact radius ( $r_1$ ).

## 4 Lifetime analysis

### 4.1 Prediction of crack growth

The cyclic crack-growth rate  $da/dN$  in a ceramic material, where  $a$  is the crack length and  $N$  is the number of load cycles, can be described by a Paris-law expression in terms of the applied stress intensity range  $\Delta K$ , the fracture toughness  $K_{Ic}$ , and two material parameters, namely,  $A^*$  and  $n$  [35]:

$$\frac{da}{dN} = A^* \left( \frac{\Delta K}{K_{Ic}} \right)^n \quad (5)$$

where  $\Delta K$  is given by

$$\Delta K = K_{I,max} - K_{I,min} \quad (6)$$

in which  $K_{I,max}$  and  $K_{I,min}$  are the maximum and minimum stress intensity factors in *mode I*, respectively. Using the load ratio  $R = \sigma_{min}/\sigma_{max} = 1 - \Delta K/K_{I,max}$  and introducing the constant  $C^* = A^*(1 - R)^n$ , Eq.(5) can be rewritten in the form [31]

$$\frac{da}{dN} = C^* \left( \frac{K_{I,max}}{K_{Ic}} \right)^n \quad (7)$$

by which the crack-growth rate  $da/dN$  is expressed as a function of the maximum stress intensity ( $K_{I,max}$ ) normalized by the fracture toughness ( $K_{Ic}$ ), which is a materials property.

Once the material parameters  $A^*$  and  $n$  have been experimentally determined, and the load ratio and  $K_{I,max}$  at a given position of the crack tip on a particular path are known, the crack-growth increment  $da/dN$  can be accordingly evaluated.

## 4.2 Calculation of the stress intensity factor

For the determination of the stress intensity factors (SIFs) ( $K_{I,max}$  and  $K_{I,min}$ ) during one loading cycle (i.e., corresponds to one complete revolution of the ceramic roller), the following procedure was adopted: The calculation of the SIF for an arbitrary time-dependent applied stress field is based on the weight function method developed by Bückner [24] and Rice [25]. Once the weight function is known for a particular crack geometry, the SIF can be determined by evaluating the weight function integral. In order to accomplish that, a suitable weight function expression, valid for the crack geometry under consideration, must be multiplied by the stress distribution of the “uncracked” body (in our case obtained from an FE analysis) and integrated over the entire crack length. The *mode I* stress intensity factor ( $K_I$ ) for a symmetrical stress field on a linear elastic body containing a crack of length  $a$  is obtained from the expression [36]

$$K_I = \int_0^a \sigma_I(x) m(x, a) dx \quad (8)$$

The local stress field  $\sigma_I(x)$  along a given path was approximated by a piecewise linear function and introduced as a table of pairs  $(x_i, \sigma_i)$ . The weight function  $m(x, a)$  was adopted from the general form developed by Sha and Yang [37]:

$$m(x, a) = \frac{2}{\sqrt{[2\pi(a-x)]}} \left[ 1 + M_1 \left(1 - \frac{x}{a}\right)^{1/2} + M_2 \left(1 - \frac{x}{a}\right) + M_3 \left(1 - \frac{x}{a}\right)^{3/2} + \dots \right. \\ \left. + M_n \left(1 - \frac{x}{a}\right)^{n/2} \right] \quad (9)$$

It was shown by Glinka and Shen [36] that the first four terms in Eq. (9) are necessary to adequately approximate the exact weight function for plane cracks in a one-dimensional stress field. Therefore, the three coefficients  $M_1, M_2$  and  $M_3$ , which basically depend on the crack geometry and not on the stress field, have to be determined to calculate the weight function  $m(x, a)$  for a particular cracked body. Glinka and Shen [36] evaluated these coefficients for an edge crack in a semi-infinite plate by fitting the weight function, analytically derived by Sih [38], and found their values to be

$$M_1 = 0.0719768, M_2 = 0.246984, \text{ and } M_3 = 0.514465 \quad (10)$$

Due to the difficulty in accurately evaluating the weight function integral, i.e., Eq.(8), a piecewise analytical integration procedure was developed by Glinka [39]. This technique was proposed for the analysis of fatigue crack growth in Kiciak et al. [40], in which the stress function is approximated by a series of linear segments (i.e., adopting a piecewise linear stress distribution).  $i$  as follows:

$$\sigma_i(x) = A_i x + B_i \quad (11)$$

where

$$A_i = \frac{\sigma_i - \sigma_{i-1}}{x_i - x_{i-1}}, \quad (12)$$

$$B_i = \sigma_{i-1} - A_i x_{i-1}$$

Therefore, the SIF contribution in each segment  $i$  is given by

$$K_{Ii} = \int_{x_{i-1}}^{x_i} (A_i x + B_i) \frac{\sqrt{2}}{\sqrt{\pi(a-x)}} \left[ 1 + M_1 \left(1 - \frac{x}{a}\right)^{1/2} + M_2 \left(1 - \frac{x}{a}\right) + M_3 \left(1 - \frac{x}{a}\right)^{3/2} \right] dx \quad (13)$$

which has to be summed over all segments along the crack length in the range  $0 \leq x \leq a$

$$K_I = \sum_{i=1}^n K_{Ii} \quad (14)$$

The closed form expression of the SIF associated with any segment  $i$ , resulting from the integration in Eq.(13), is given by

$$K_{Ii} = \sqrt{\frac{2a}{\pi}} [\alpha_i (C_{1i} + M_1 C_{2i} + M_2 C_{3i} + M_3 C_{4i}) + \beta_i (C_{5i} + M_1 C_{6i} + M_2 C_{7i} + M_3 C_{8i})] \quad (15)$$

where  $\alpha_i = B_i + aA_i$  and  $\beta_i = -aA_i$ , and

$$\begin{aligned} C_{1i} &= 2 \left[ \left(1 - \frac{x_{i-1}}{a}\right)^{1/2} - \left(1 - \frac{x_i}{a}\right)^{1/2} \right], \quad C_{2i} = \left[ \left(1 - \frac{x_{i-1}}{a}\right) - \left(1 - \frac{x_i}{a}\right) \right] \\ C_{3i} &= \frac{2}{3} \left[ \left(1 - \frac{x_{i-1}}{a}\right)^{3/2} - \left(1 - \frac{x_i}{a}\right)^{3/2} \right], \quad C_{4i} = \frac{1}{2} \left[ \left(1 - \frac{x_{i-1}}{a}\right)^2 - \left(1 - \frac{x_i}{a}\right)^2 \right] \\ C_{5i} &= \frac{2}{5} \left[ \left(1 - \frac{x_{i-1}}{a}\right)^{5/2} - \left(1 - \frac{x_i}{a}\right)^{5/2} \right], \quad C_{6i} = \frac{1}{3} \left[ \left(1 - \frac{x_{i-1}}{a}\right)^3 - \left(1 - \frac{x_i}{a}\right)^3 \right] \end{aligned} \quad (16)$$

The stresses normal to the prospective crack plane were obtained from the nodal FE data along paths from the surface down to a predefined depth in the ceramic roller as illustrated in Fig. 2. The FE model that showed quite acceptable accuracy compared to the analytical solution in addition to a

manageable model size (*Mesh03*, refer to Section 5.2) was selected for post-processing and further extraction of nodal data.

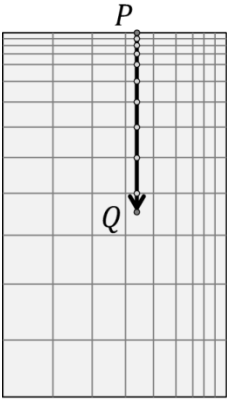


Fig. 2. Crack growth path into the depth of the ceramic roller

The stresses were initially extracted from a reference path  $\overline{P_0Q_0}$  in the radial direction  $\rho$  and further on along the paths  $\overline{PQ}$  in planes rotated by angular increments  $\Delta\phi$  in the circumferential direction  $\Phi$  as shown in Fig. 3.

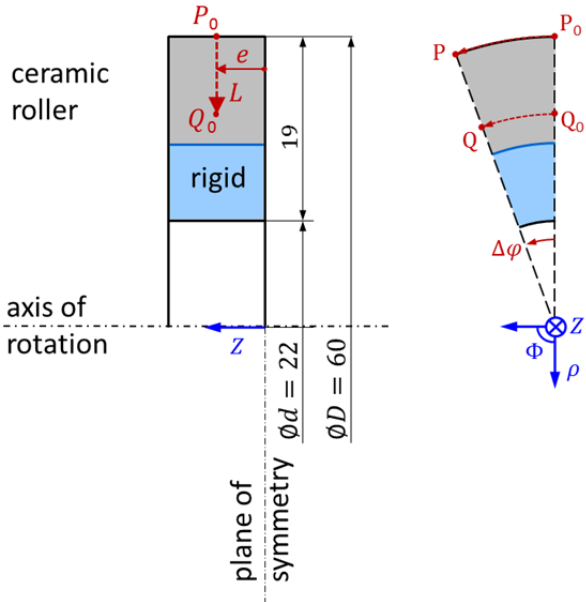


Fig. 3. Path to extract stresses; outer diameter: 60 mm, inner diameter: 22 mm

Stresses at intermediate positions were linearly interpolated. The path was defined as a function of the variables  $e$  and  $L$  along the axial  $Z$  and radial  $\rho$  directions, respectively, and the angular position variable  $\varphi$  in the circumferential direction  $\Phi$ , Fig. 3.

Using an optimization algorithm, the path positions with local and global stress maxima were identified at positions where macroscopic crack formation in the ceramic roller is expected according to experimental observations. The stresses on material points in a single load cycle were obtained from a series of path evaluations with a fixed axial position  $e$  by incrementally increasing the angular position  $\varphi$ .

The following assumptions apply to the SIF calculations:

- The maximum principal stress is tangential to the surface and much higher than surface shear stresses, hence, both crack formation and crack propagation occur perpendicular to the surface, see Fig. 2; this assumption was experimentally verified;
- a half-space approximation was adopted for the surface crack model (i.e., surface radius is much larger than the crack depth);
- crack growth is nearly planar (large radius of curvature of stress isolines);
- long and slightly curved cracks were modeled as edge cracks.

## 5 Results

### 5.1 Experimental results

The  $da/dN$  curves measured by cyclic bending fatigue tests under different conditions are shown in Fig. 4. Comparing the data in air at different load ratios, one sees that the  $da/dN$  curves for both load ratios show almost the same slope. The crack-growth rate is higher for  $R = -1$  (empty circles) than  $R = 0.1$  (empty triangles). In other words, to maintain the same crack-growth rate, a much lower  $K_{I,max}$  is needed under alternating load compared to fluctuating tensile load. The exponent  $n$  (slope of the  $da/dN$  curve) for tests run at  $R = 0.1$  in water (filled triangles) is smaller than that for tests run

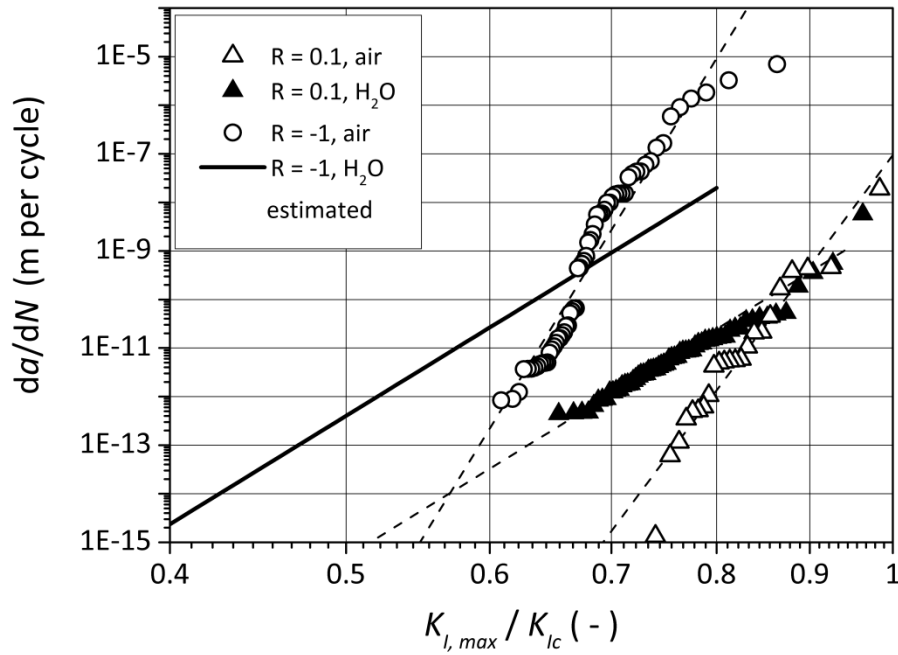


Fig. 4.  $da/dN$  curves obtained from four-point-bending cyclic fatigue tests on SN-GP black;  $f=40$  Hz

in air (empty triangles), which points out to the presence of a different (or additional) mechanism that promotes crack growth and indicates higher material susceptibility to crack growth in water. It can be assumed that the same behavior, similar to that in air, is present under alternating load in water, however, it appears at a lower  $K_{I,max}$ . Consequently, a  $da/dN$  curve for  $R = -1$  in water was estimated to follow the solid line plotted in Fig. 4. The straight lines in Fig. 4 represent fitted data obtained from the Paris law, Eq.(5) and (7).

The parameters of the Paris laws for  $R = 0.1$  and  $R = -1$  in water are summarized in Table 4.

Table 4. Four-point-bending cyclic fatigue material parameters for silicon nitride SN-GP black in water, Eq.(5) and (7)

Parameter	R = 0.1	R = -1.0
	Fit of experimental data (filled triangles in Fig. 4)	Estimated (solid line in Fig. 4)
$A^*$ [m/cycle]	$4.689 \times 10^{-8}$	$4.0 \times 10^{-13}$
$n$	23	23
$C^*$ [m/cycle]	$4.156 \times 10^{-9}$	$3.355 \times 10^{-6}$

The coefficient of friction was calculated by measuring the torque generated in rolling contact; the mean values obtained for each applied normal load are shown in Fig. 5.

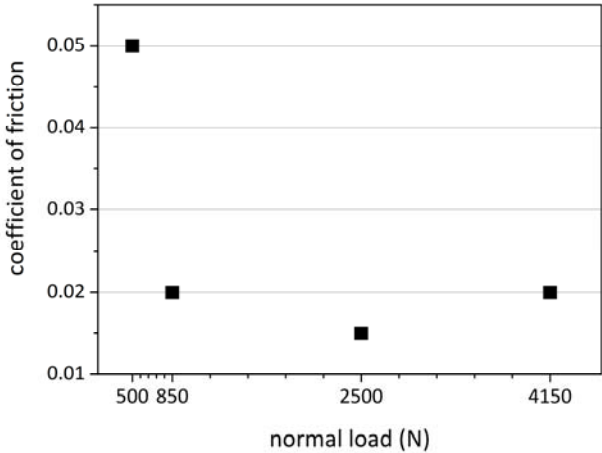


Fig. 5. Coefficient of friction in lubricated rolling-contact experiments with SKF TT9 oil

Crack formation was experimentally observed by means of RCF evolution experiments (detailed results are found elsewhere [41]). Cracks were detected only for the highest applied normal load (i.e.,  $F_N=4150$  N). Initial surface crack formation was recorded after  $N=7500$  load cycles (rotations); all samples showed cracks by  $N=2 \times 10^6$  load cycles.

Fig. 6 shows the morphology of the cracks observed on the surface and in the subsurface after  $10^7$  load cycles. The schematic drawing shown on the left illustrates the contact ellipse, the developed rolling (wear) track along the surface of the ceramic roller, and the location of surface crack formation. The light microscope image (middle) shows microspalls and cracks on the surface and the scanning electron microscope (SEM) image (right) shows the results of a cross-sectional analysis depicting crack propagation in the radial direction in the depth.

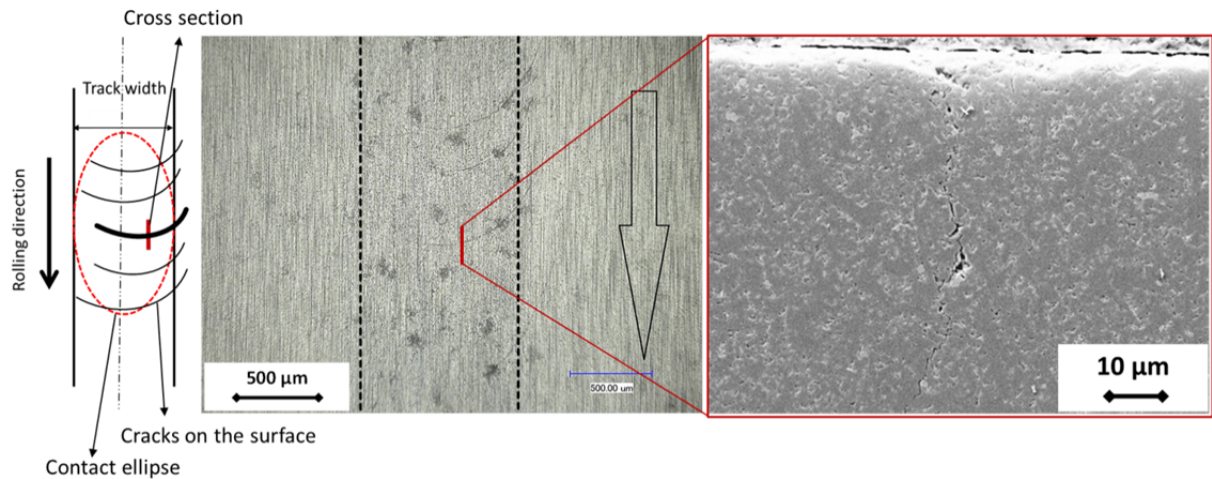


Fig. 6. (left) Top view of a wear track on the ceramic roller showing an ideal elliptical contact patch, surface cracks, and the location of the cross-sectional polished section; (middle) light microscope image showing a wear track with microspalls and cracks; (right) SEM image showing crack propagation in the radial direction in the depth;  $F_N=4150$  N,  $N=10^7$  cycles

## 5.2 Mesh refinement

The parametric study conducted to achieve a reasonable mesh refinement level was based on the load case  $F_N=500$  N. The peak tensile stress value obtained from the Hertzian solution, Eq. (1), for this case is  $\sigma_{r1}=491.2$  MPa. Selecting a rather low value for the applied normal load ( $F_N=500$  N) ensures a reasonable comparison between the FEM solution and the Hertzian solution which assumes that strains in the contact region are sufficiently small to lie within the scope of the linear theory of elasticity.

Fig. 7 and Fig. 8 show the FEM calculated maximum principal stress ( $S_{max}$ ) on the surface and in the depth of the ceramic roller for  $F_N=500$  N for different mesh refinement levels (refer to Table 3). The plot indicates that the peak of  $S_{max}$  is dependent on the mesh density.

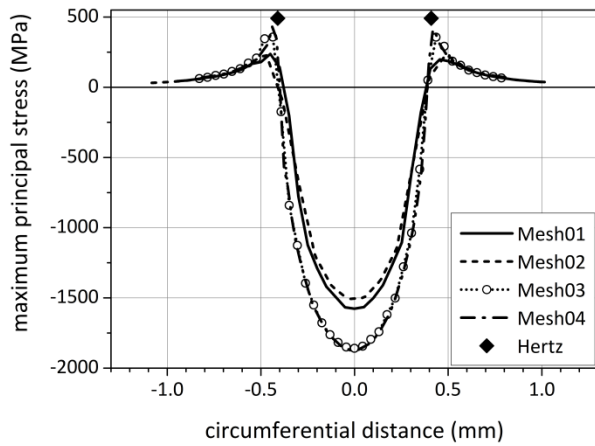


Fig. 7.  $S_{\max}$  on the surface of the ceramic roller obtained along the contact ellipse's major axis for different mesh densities and compared to the value of  $\sigma_{r1}$  in Eq.(1);  $F_N=500$  N,  $\mu=0.05$

The highest difference between the FEM calculated maximum principal stress ( $S_{\max}$ ) using *Mesh03* and *Mesh04*, and the Hertzian solution ( $\sigma_{r1}$ ) is 20% and 15%, respectively.

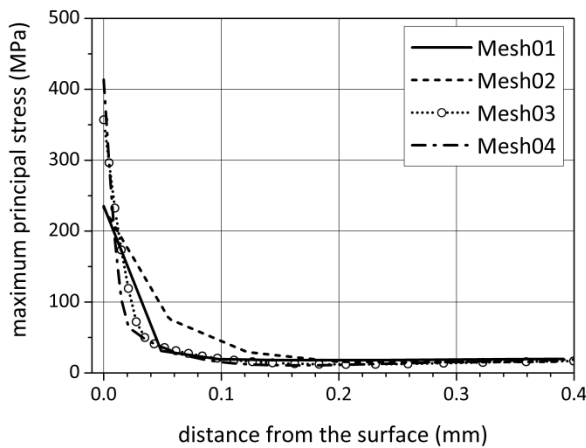


Fig. 8.  $S_{\max}$  in the depth of the ceramic roller obtained along the contact ellipse's major axis for various mesh densities;  $F_N=500$  N,  $\mu=0.05$

As shown in Fig. 8, a steep tensile stress gradient appears in the depth of the material; almost 50  $\mu$ m below the surface, the tensile stress drops to below 10% of its peak value that appears on the surface.

### 5.3 Fully-elastic model

The locations with highest tensile stresses in the simulations were identified as shown in the FEM-generated contour plots of  $S_{\max}$  in Fig. 9. The maximum stressed sites served in determining possible

crack paths for further SIF and crack-growth rate calculations.

For the cases  $F_N=500$  N (corresponding to a maximum Hertzian contact pressure of 3.0 GPa, Eq. (3)),  $F_N=850$  N (3.5 GPa), and  $F_N=2500$  N (5.0 GPa) the maximum calculated stress intensity factor was well below the measured fracture toughness ( $K_{Ic,water}=5.39$  MPa·m<sup>1/2</sup>), thus, indicating that both crack formation and fracture are unlikely to occur under such loads.

For  $F_N=4150$  N (corresponding to a maximum Hertzian contact pressure of 6.0 GPa) two critical paths were identified: (i) at an axial position  $e=0.0$  mm (corresponds to the contact ellipse's major axis: Path A in Fig. 9d), and (ii) at an axial position  $e=0.42$  mm (corresponds to a distance almost equal to the ellipse's minor radius: Path B Fig. 9d). The load history during a load cycle (rotation) can be evaluated for the predicted crack-growth paths by extracting stresses in the direction indicated by the white dotted arrows as shown in Fig. 9d.

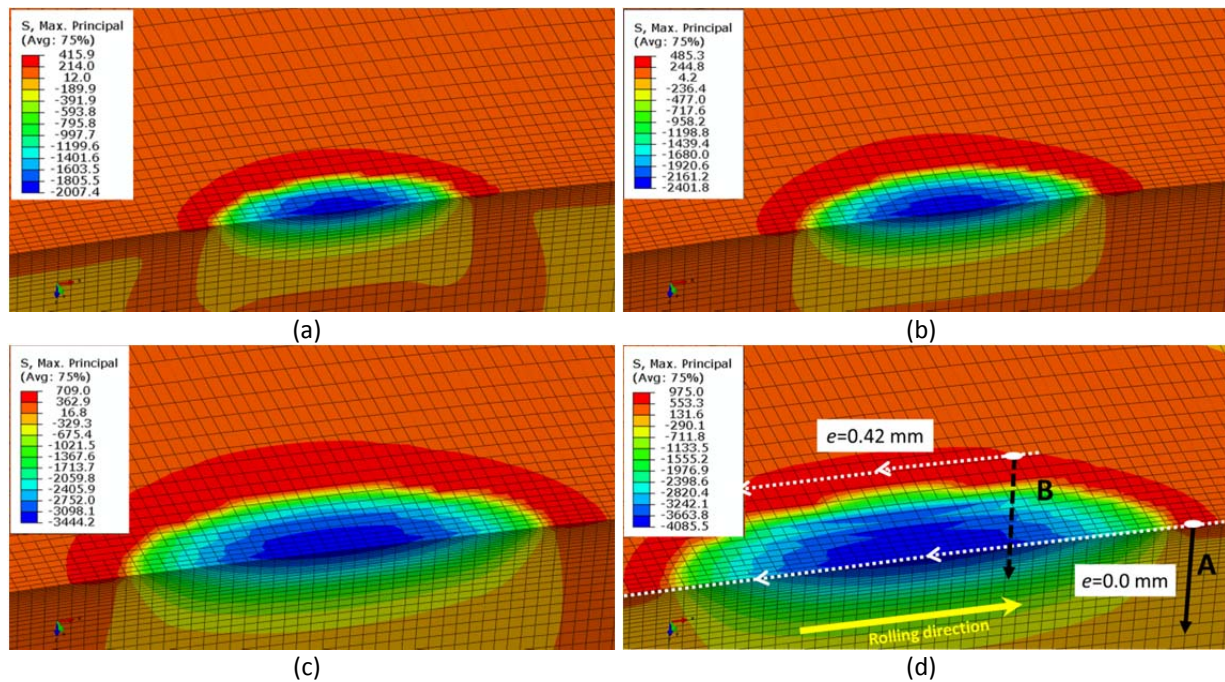


Fig. 9. FEM-generated contour plots of  $S_{max}$  (fully-elastic model) at an applied normal loads of (a) 500 N, (b) 850 N, (c) 2500 N, and (d) 4150 N. Highest stress values identified at the following axial positions from the plane of symmetry: (a)  $e=0.0$  mm and  $e=0.22$  mm, (b)  $e=0.0$  mm and  $e=0.26$  mm, (c)  $e=0.0$  mm and  $e=0.42$  mm, and (d)  $e=0.0$  mm and  $e=0.42$  mm; white dotted arrows in (d) indicate the path of interest travelled in a single load cycle corresponding to a specific axial positions  $e$ ; black arrows indicate crack-growth paths into the depth

In a single load cycle, points along Path A that are above or ca. 300  $\mu\text{m}$  in depth undergo alternating loading (Fig. 10a); for the calculation of crack growth along this path, the experimental data for  $R = -1$  was used. Points on Path B undergo fluctuating loading in tension (Fig. 10b); for crack-growth calculations in these cases, the experimental data for  $R = 0.1$  was applied.

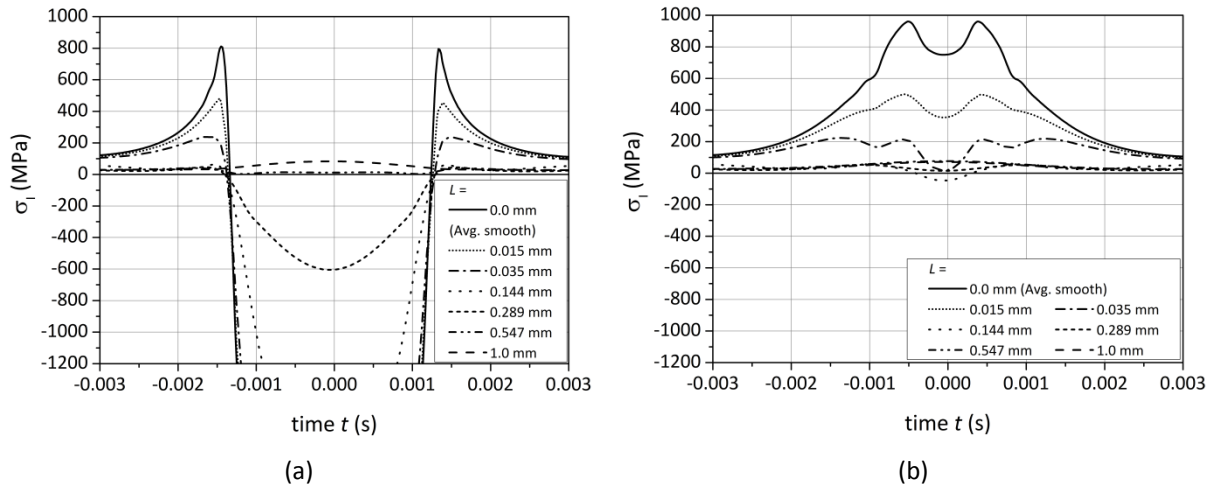


Fig. 10. Load history along (a) Path A at  $e=0.0$  mm, and (b) Path B at  $e=0.42$  mm, according to Fig. 9d, each line represents a position in the depth given by the value of  $L$  in the legend;  $F_N=4150$  N,  $\mu=0.02$ , fully-elastic model

Fig. 11 shows the SIFs ( $K_{I,max}$  and  $K_{I,min}$ ) normalized by the fracture toughness ( $K_{IC}$ ) as function of the crack length along both Path A and Path B.

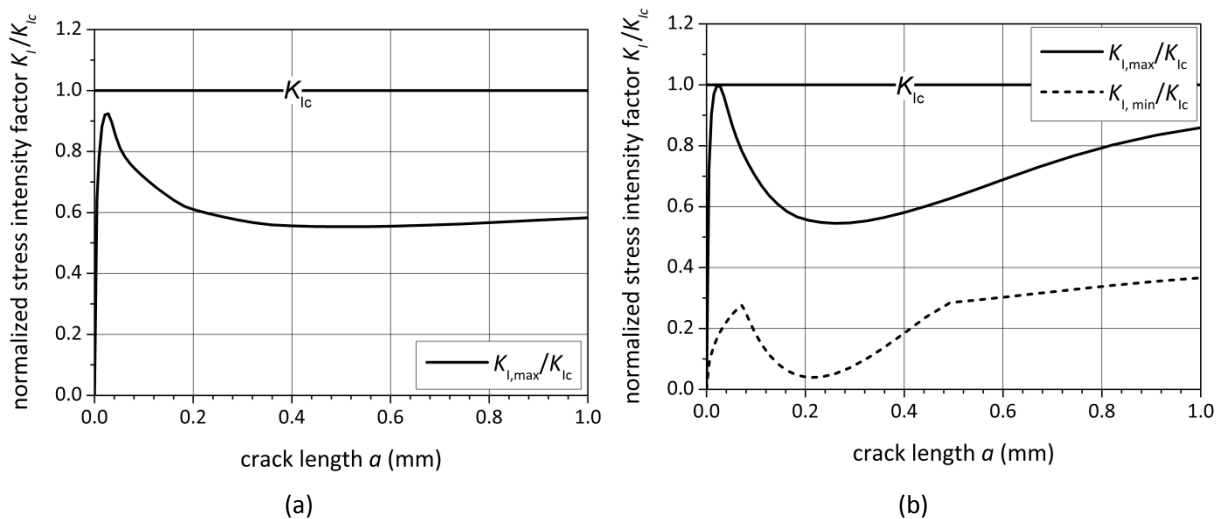


Fig. 11. SIF normalized by the fracture toughness  $K_{IC}$  as function of the crack length, (a)  $e=0.0$  mm, (b)  $e=0.42$  mm;  $F_N=4150$  N,  $\mu=0.02$ ,  $K_{IC} = K_{IC,water}$ , fully-elastic model, edge-crack approximation. Note that  $K_{I,min}$  on Path A ( $e=0.0$  mm) is negative and thus, not shown in the graph

As depicted in Fig. 11 that the maximum SIF is always below the fracture toughness of the material. Therefore, no unstable crack growth will occur. Crack propagation will, however, take place due to fatigue crack growth. The crack-growth behavior (crack length versus number of load cycles) is shown in Fig. 12.

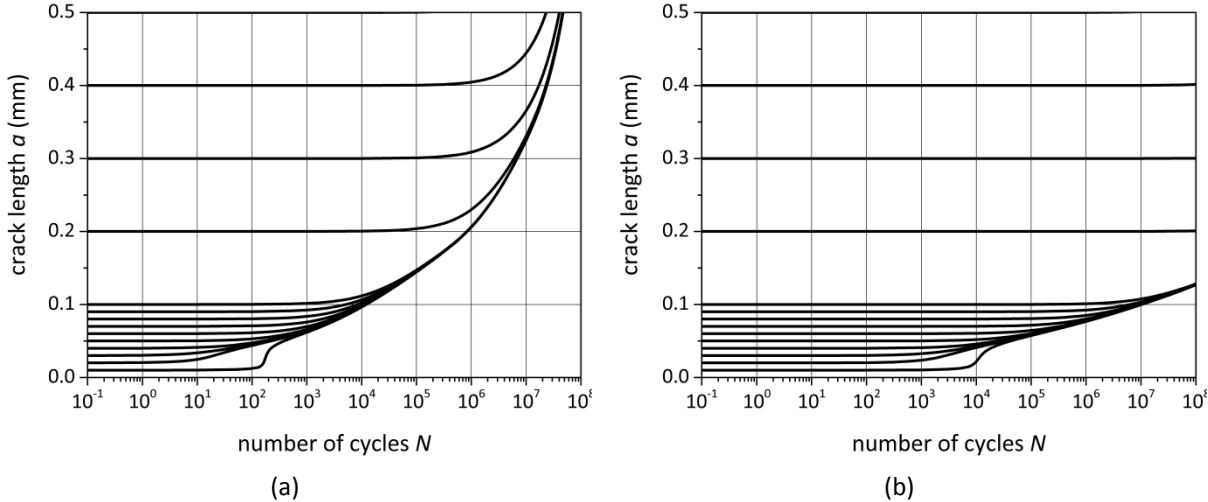


Fig. 12. Crack length in the depth of the ceramic roller as a function of the number of load cycles, (a) Path A:  $e=0.0$  mm, (b) Path B:  $e=0.42$  mm;  $F_N=4150$  N,  $\mu=0.02$ , fully-elastic model. Each line represents the growth behavior of cracks with a predefined initial length:  $10\ \mu\text{m}$ , ...,  $400\ \mu\text{m}$

Small cracks (ca.  $10\ \mu\text{m}$  in the depth) are expected to considerably propagate in the few hundred load cycles succeeding  $N=10^2$  along Path A (located at an axial position of  $e=0.0$  mm from the plane of symmetry), Fig. 12a, and in the few thousand load cycles succeeding  $N=10^4$  along Path B (located at an axial position of  $e=0.42$  mm from the plane of symmetry), Fig. 12b. Cracks along Path B will, however, eventually stop once they reach an approximate length of  $a=130\ \mu\text{m}$ . Nonetheless, continued fatigue crack growth is predicted along Path A.

### 5.4 Elastoplastic model

A comparison between the FE simulations carried out with a fully-elastic material behavior and the ones with an elastoplastic material is shown in Fig. 13 and Fig. 14 in terms of the maximum contact stress (CPRESS) and the surface maximum principal stress ( $S_{\text{max}}$ ) along the contact major axis, respectively.

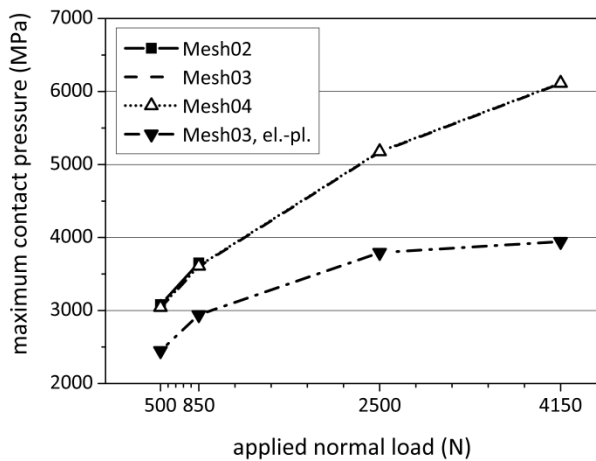


Fig. 13. Maximum contact pressure on the surface of the ceramic roller as a function of the applied normal load

Fig. 13 shows that the contact pressure is independent of the mesh density. On the other hand, it depicts a distinct reduction in its values when plastic deformation is incorporated into the model.

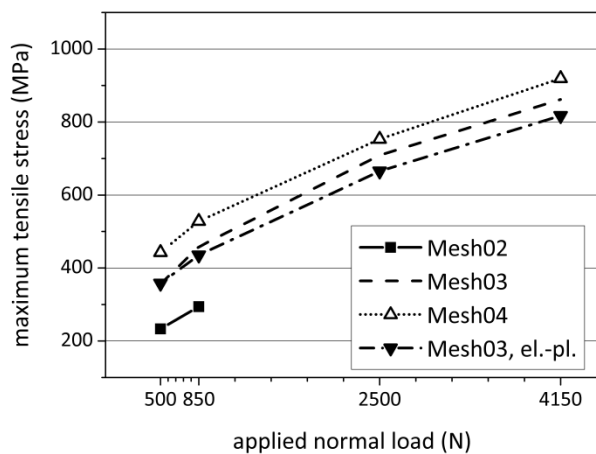


Fig. 14. Maximum surface tensile stresses along the contact ellipse's major axis as a function of the applied normal load

Fig. 14 indicates that surface tensile stresses are mesh dependent; whereas, the reduction in stresses due to plastic deformation (observed for the same mesh density) is merely pronounced at higher loads (i.e.,  $F_N=2500$  N and  $F_N=4150$  N).

Post-processing of the elastoplastic model was done only for  $F_N=4150$  N, which is the only critical case relevant to crack growth. The FEM-generated contour plots of  $S_{max}$  for the fully-elastic and elastoplastic models at  $F_N=4150$  N are show in Fig. 15. The axial position from the plane of symmetry ( $e$ ),

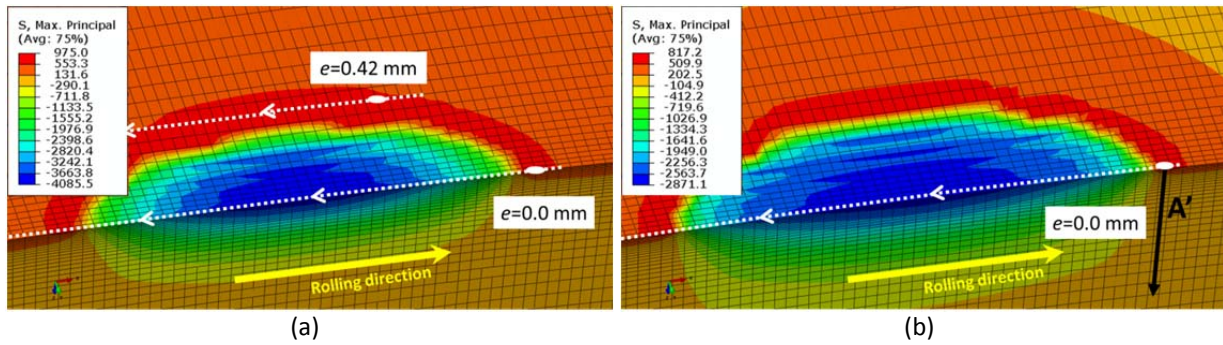


Fig. 15. FEM-generated contour plots of  $S_{\max}$  for (a) fully-elastic model, and (b) elastoplastic model;  $F_N=4150$  N,  $\mu=0.02$ . Highest stress values identified at the following axial positions from the plane of symmetry: (a)  $e=0.0$  mm and  $e=0.42$  mm, and (b)  $e=0.0$  mm and  $e=0.55$  mm; white dotted arrows indicate the critical path under consideration travelled in a single load cycle corresponding to a specific axial positions  $e$ ; black arrows indicate crack-growth paths into the depth

at which the peak stress appears, is indicated on the contour plots with white dots.

The plastic deformation undergone in the steel disk results in a larger contact area (by ca. 25% for  $F_N=4150$  N) and reduced tensile stresses. A single critical path, at an axial position of  $e=0.0$  mm (Path A' in Fig. 15b), was identified for the elastoplastic model.

The loading history along Path A', as identified in Fig. 15b, is shown in Fig. 16.

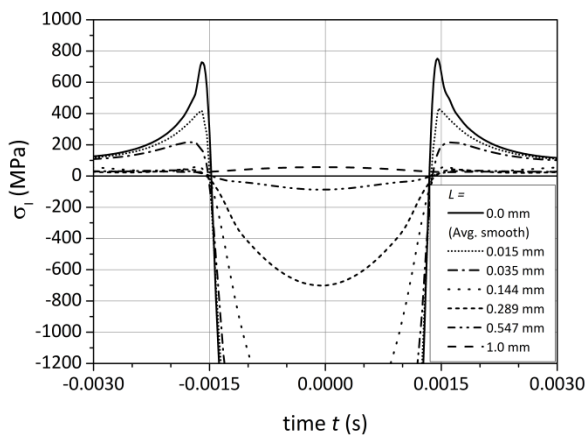


Fig. 16. Load history along Path A' at  $e=0.0$  mm, according to Fig. 15b, each line represents a position in the depth given by the value of  $L$  in the legend;  $F_N=4150$  N,  $\mu=0.02$ , elastoplastic model

Points along Path A' above ca. 300  $\mu$ m in the depth undergo alternating tension-compression stress.

The normalized SIF as a function of crack length along Path A' is shown in Fig. 17. As expected, the

lower stresses when considering plastic deformation resulted in lower SIFs.

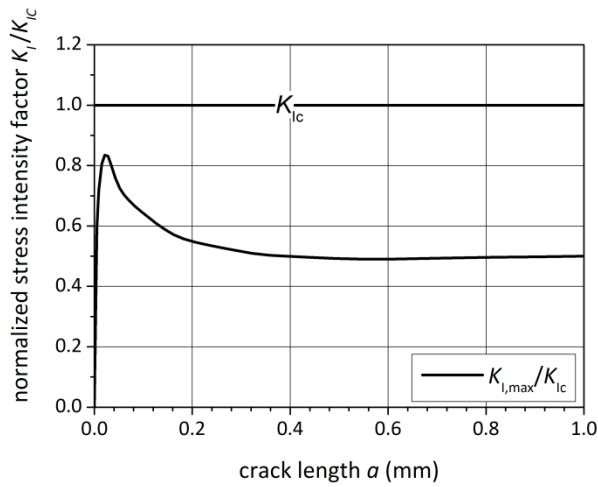


Fig. 17. IF normalized by the fracture toughness  $K_{IC}$  as function of the crack length along Path A' at  $e=0.0$  mm;  $F_N=4150$  N,  $\mu=0.02$ ,  $K_{IC} = K_{IC,water}$ , elastoplastic model, edge-crack approximation

Consequently, the crack-growth behavior (crack length as a function of the number of load cycles) is shown in Fig. 18.

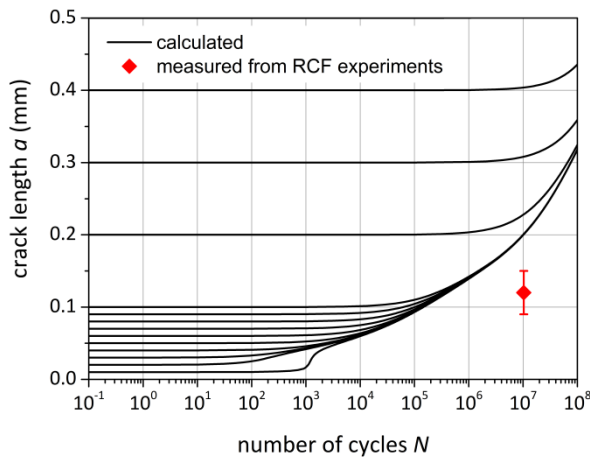


Fig. 18. Crack length in the depth of the ceramic roller as a function of the number of load cycles along Path A' at  $e=0.0$  mm;  $F_N=4150$  N,  $\mu=0.02$ , elastoplastic model. Each line represents the growth behavior of cracks with a predefined initial length: 10  $\mu$ m, ..., 400  $\mu$ m. Experimentally, crack lengths were measured at  $N=10^7$  load cycles. The figure indicates that small cracks (ca. 10  $\mu$ m in depth) are expected to considerably propagate in one to two thousand load cycles following  $N=10^3$ ; continued fatigue crack growth is expected afterwards. For such small cracks, the crack length at  $10^7$  load cycles is estimated to reach  $a=200$   $\mu$ m;

whereas, crack lengths measured in the RCF experiments at  $10^7$  load cycles were found to lie within the range  $a=120\pm 30$   $\mu\text{m}$ , Fig. 18.

## 6 Discussion

In the RCF experiments, surface cracks appeared in the contact zone after reaching a threshold value in the applied normal load. Crack formation was not instantaneous (i.e., does not occur upon initial contact) and telltale signs of crack propagation – on the surface and into the depth of the ceramic samples as shown in Fig. 6 – were observed with an increasing number of load cycles, thus, indicating fatigue crack growth. The observation that crack formation is not symmetric about the rolling track, as depicted in the light microscope image in Fig. 6, can be traced to the fact that the slightest misalignment in the setup would cause a disturbance in the symmetry of contact stresses, thus, leading to a preferential direction for crack propagation.

As depicted in Fig. 11, the calculation SIFs for hypothetical cracks resulted in somewhat smaller  $K_{I,max}/K_{IC}$  along Path A ( $e=0.0$  mm) than Path B ( $e=0.42$  mm). Nonetheless, earlier crack propagation was predicated along Path A (Fig. 12a and b). Small and superficial cracks in Path A experience alternating stresses unlike cracks in Path B, which undergo pure tensile stresses. Experimentally, the bending cyclic fatigue tests resulted in cracks growth approximately three orders of magnitude faster under fully-reversed alternating load ( $R = -1$ ) than under fluctuating tensile load ( $R = 0.1$ ) as depicted in the  $da/dN$  curves shown in Fig. 4. This is well reflected by the constant  $C^*$  in the modified Paris law in Eq.(7), which indicates that the load severity is determined by the combination of both the tensile stress magnitude on the surface and load history. Hence, regions with alternating stresses are expected to experience more severe crack growth (see [31, 42]) and thus, suffer more pronounced damage in the microstructure than regions experiencing fluctuating tensile stresses.

Based on the stresses extracted from the fully-elastic model, the crack-growth behavior of short cracks (ca.  $10$   $\mu\text{m}$  in depth) for the highest applied load (i.e.,  $F_N=4150$  N) indicates significant fatigue crack growth along Path A ( $e=0.0$  mm) after undergoing ca.  $10^2$  load cycles (Fig. 12a). Under the same load, crack growth along Path B ( $e=0.42$  mm) is predicted for short cracks after ca.  $10^4$  load cycles and

continues until reaching a crack length of  $a=130\ \mu\text{m}$ , after which crack growth is expected to reach an arrest (Fig. 12b). On the other hand, based on the results of the elastoplastic model, fatigue crack growth is predicted only along Path A' ( $e=0.0\ \text{mm}$ ) and after undergoing a higher number of load cycles, namely, ca.  $N=10^3$  load cycles (compare Fig. 12a and Fig. 18). Plastic deformation in the steel disk reduces the stresses developed in contact; plastic strains in one of the contacting bodies modify the contact surface geometry and, thus, attenuate non-conforming contact conditions. This results in an increase in the contact area and a reduction in contact stresses (Fig. 13). Consequently, the SIF as a function of crack length will be slightly lower when plastic deformation is taken into consideration. Unstable crack growth for small cracks is expected once the normalized SIF exceeds 1.0. In Fig. 11b for the fully-elastic calculation, the normalized SIF barely reaches 1.0, while for the more realistic elastoplastic case it is considerably smaller. It can, thus, be concluded that unstable crack growth may be ruled out here.

The lifetime predictions based on the FE model with elastoplastic material behavior were closer to the experimental results than those based on the more simplified fully-elastic model. Considering plasticity in a mechanical contact simulation may yield more realistic results, however, the added complexity to the system under consideration may be justified only in certain cases. For instance, in our case it can be argued that incorporating plasticity will affect the accuracy of the solution only for high loads (refer to Fig. 14). Moreover, it should be stated that the isotropic plasticity model was adopted in the FE simulations conducted herein for its simplicity; more suitable plasticity models may be able to more accurately capture plastic strains in the state of incipient yield expected in rolling contact.

Experimentally, crack formation was detected for  $F_N=4150\ \text{N}$  between  $N=7500$  and  $N=2\times 10^6$  load cycles. The crack-growth calculations assume the presence of pre-existing flaws with a minimum size of  $10\ \mu\text{m}$ . This crack length is a limitation imposed by the smallest element size in the FE mesh. The formation of such cracks from much smaller microstructural imperfections like "snowflakes" [43, 41] or micro-spalls (visible in Fig. 6) is difficult to capture with the present method but may well be the

reason for the deviation between calculations and experimental observations.

It is, however, worth noticing that even by relying on a coarse mesh (*Mesh03*) for calculating stresses and thus, resulting in underestimated stress magnitudes (lower by 20% compared to the Hertzian solution and by 5% compared to *Mesh04*, see Fig. 7), the calculated lifetimes lied within the lower range of the experimental results. In other words, it might be even argued that the applied method is somewhat conservative in predicting component lifetimes through estimation of crack length. For instance, Fig. 18 indicates a minimum overestimation of calculated crack length by 33% at  $N=10^7$ .

The weight function given in Eq. (9) was found to be among the most universal weight function forms and can be fitted with accuracy better than 1% into several one-dimensional edge cracks of any depth [36]. A much more complicated approximation for shallow semi-elliptical surface cracks in finite thickness plates is provided by Wang and Lambert [44], who indicated accuracy better than 3% compared to FEM data. For the same depth, the edge crack approximation leads to an upper limit for the SIF and consequently, finds the most conservative lifetime prediction. In this work, only edge cracks and the weight function shown in Eq. (6) were employed to calculate SIFs for the twin-disk experiment. As long as surface cracks in the ceramic roller are small compared to the contact area they can be handled as plane cracks in a semi-infinite plate, where the crack is loaded with a one-dimensional stress field. With increasing crack size the deviation from real crack geometry and loading increases. Therefore, the evaluations are limited to cracks of less than 500  $\mu\text{m}$  in depth.

## 7 Conclusions

In this study, we proposed a method for the prediction of fatigue life of structural ceramics undergoing rolling contact. Lifetime predictions were based on material data obtained from four-point-bending cyclic fatigue tests and stresses obtained from finite element analysis. The following conclusions can be drawn:

The incorporation of plastic deformation in the stress analysis resulted, as expected, in lower stresses and consequently lower SIFs. The experimental observations were closer to the predictions of the model that relied on elastoplastic material behavior.

Early crack propagation was predicated in locations experiencing fully-reversed alternating load in comparison to fluctuating tensile load; the crack-growth rate is strongly dependent on the stress magnitude and type of applied cyclic load.

The method presented in this study enabled calculating fatigue life for ceramic components subjected to complex loading situations; it rendered results that are in accordance with experimental observations. However, crack-growth rates were shown to be overestimated. This presented method can be applied whenever crack paths are known. Nevertheless, prior knowledge of relevant environmental conditions (temperature, humidity, etc.) and type of loading (fluctuating, fully-reversed, etc.) is indispensable for the proper determination of a crack-growth law.

While beyond the scope of this study, consideration of environment effects on the fatigue crack growth of ceramics suggests that the life of ceramic components is strongly affected by the surrounding environment and especially humidity.

## 8 Acknowledgements

The research leading to these results has received funding from the European Union's Seventh Framework Program FP7/2007-2013 under grant agreement no. 263476.

## 9 Bibliography

- [1] X. Zhao, J. Liu, B. Zhu, H. Miao and Z. Luo, "Friction and wear of Si<sub>3</sub>N<sub>4</sub> ceramic/stainless steel sliding contacts in dry and lubricated conditions," *Journal of Materials Engineering and Performance*, vol. 2, no. 6, pp. 203-208, 1997.
- [2] P. Reis, J. Davim, X. Xu and J. Ferreira, "Friction and wear behaviour of B-silicon nitride–steel couples under unlubricated," *Materials Science and Technology*, vol. 22, no. 2, pp. 247-252, 2006.
- [3] M. Hadfield, "Rolling Contact Fatigue of Ceramics," Brunel University, 1993.
- [4] M. Hadfield, T. Stolarski and R. Cundill, "Failure modes of ceramics in rolling contact," *Proceedings of the Royal Society of London - Series A*, vol. 443, no. 1919, pp. 607-621, 1993.
- [5] W. Wang, "Rolling Contact Fatigue of Silicon Nitride," Bournemouth University, 2010.
- [6] Z. Jing-ling, C. Xiao-yang, Z. Pei-zhi and W. Guo-qing, "Rolling contact fatigue of silicon nitride balls under pure rolling condition," in *Advanced Tribology: Proceedings of CIST2008 & ITS-IFTtoMM2008*,

Beijing, China, 2010.

- [7] M. Härtelt, H. Riesch-Oppermann, I. Khader and O. Kraft, "Probabilistic lifetime prediction for ceramic components in rolling applications," *Journal of the European Ceramic Society*, vol. 32, p. 2073–2085, 2012.
- [8] R. Hanzal, "Rolling Contact Fatigue Failures in Silicon Nitride and their Detection," University of Southampton, 2013.
- [9] R. Ritchie, "Mechanisms of fatigue crack propagation in metals, ceramics and composites: Role of crack tip shielding," *Materials Science and Engineering, A*, vol. 103, pp. 15-28, 1988.
- [10] S. Fünfschilling, "Mikrostrukturelle Einflüsse auf das R-Kurvenverhalten bei Siliciumnitridkeramiken," KIT Scientific Publishing, Karlsruhe, 2009.
- [11] S. Suresh, *Fatigue of Materials*, 2nd ed., Cambridge University Press, 2004.
- [12] R. Dauskardt, "A frictional-wear mechanism for fatigue-crack growth in grain bridging ceramics," *Acta Metallurgica et Materialia*, vol. 41, no. 9, p. 2765–2781, 1993.
- [13] R. Ritchie and M. Launey, "Crack growth in brittle and ductile solids," in *Encyclopedia of Tribology*, Q. J. Wang and Y. Chung, Eds., Boston, MA, Springer US, 2013, pp. 596-605.
- [14] R. Dauskardt, M. James, J. Porter and R. Ritchie, "Cyclic fatigue-crack growth in a SiC-whisker-reinforced alumina ceramic composite: Long- and small-crack behavior," *Journal of the American Ceramic Society*, vol. 75, no. 4, p. 759–771, 1992.
- [15] C. Gilbert, J. Cao, W. Moberlychan, L. DeJonghe and R. Ritchie, "Cyclic fatigue and resistance-curve behavior of an in situ toughened silicon carbide with Al-B-C additions," *Acta Materialia*, vol. 44, no. 8, p. 3199–3214, 1996.
- [16] Liu, S.-Y. and I.-W. Chen, "Fatigue of yttria-stabilized zirconia: I, fatigue damage, fracture origins, and lifetime prediction," *Journal of the American Ceramic Society*, vol. 74, no. 6, pp. 1197-1205, 1991.
- [17] S.-Y. Liu and I.-W. Chen, "Fatigue of yttria-stabilized zirconia: II, crack propagation, fatigue striations, and short-crack behavior," *Journal of the American Ceramic Society*, vol. 74, no. 6, pp. 1206-1216, 1991.
- [18] D. Jacobs and I.-W. Chen, "Cyclic fatigue in ceramics: A balance between crack shielding accumulation and degradation," *Journal of the American Ceramics Society*, vol. 78, no. 3, pp. 513-520, 1995.
- [19] C. Gilbert and R. Ritchie, "Transient fatigue-crack growth behavior following variable-amplitude loading in a monolithic silicon nitride ceramic," *Engineering Fracture Mechanics*, vol. 60, no. 3, pp. 303-313, 1998.
- [20] T. Lube, I. Khader, A. Kailer, U. Degenhardt and K. Berroth, "Ermüdungsbruch in Siliziumnitrid," S. Mayer, M. Panzenböck and H. Clemens, Eds., Bonn, Praktische Metallographie Sonderband, INVENTUM GmbH, 2014, pp. 353-357.
- [21] P. Paris and F. Erdogan, "A critical analysis of crack propagation laws," *Journal of Basic Engineering*, vol. 85, no. 4, pp. 528-533, 1963.

- [22] T. Fett and D. Munz, *Stress Intensity Factors and Weight Functions*, Southampton: WIT Press, 1997.
- [23] T. Fett, *Stress Intensity Factors – T-Stresses – Weight Functions*, Karlsruhe: Universitätsverlag Karlsruhe, 2008, pp. 27-33.
- [24] H. Bückner, "A novel principle for the computation of stress intensity factors," *Zeitschrift für Angewandte Mathematik und Mechanik ZAMM*, vol. 50, pp. 529-546, 1970.
- [25] J. Rice, "Some remarks on elastic crack-tip stress fields," *International Journal of Solids and Structures*, vol. 8, no. 6, pp. 751-758, 1972.
- [26] M. Lengauer and R. Danzer, "Silicon nitride tools for the hot rolling of high-alloyed steel and superalloy wires – Crack growth and lifetime prediction," *Journal of the European Ceramic Society*, vol. 28, no. 11, pp. 2289-2298, 2008.
- [27] *EU-FP7-NMP, Enhanced reliability and lifetime of ceramic components through multi-scale modelling of degradation and damage RoliCer, ID: 263476*, 2011-2014.
- [28] EN 843-1, *Advanced Technical Ceramics - Mechanical properties of monolithic ceramics at room temperature: Part 1 - Determination of Flexural Strength*, 2006.
- [29] CEN EN 14425-5, *Fine Ceramics (Advanced Ceramics, Advanced Technical Ceramics) – Test methods for fracture toughness of monolithic ceramics -- Single-edge V-notch beam (SEVNB) method*, 2005.
- [30] C. von der Wehd, T. Lube, I. Khader, A. Kailer, U. Degenhardt and K. Berroth, "Zyklische Ermüdung technischer Keramiken in wässrigen Medien," in *Fortschritte in der Werkstoffprüfung für Forschung und Praxis*, Düsseldorf, 2013.
- [31] D. Munz and T. Fett, *Ceramics*, Berlin, Heidelberg: Springer, 1999.
- [32] I. Khader, D. Kürten and A. Kailer, "A study on the wear of silicon nitride in rolling–sliding contact," *Wear*, vol. 296, p. 630–637, 2012.
- [33] D. Kürten, "Einfluss der tribochemischen Schmierstoffoxidation auf die wasserstoffinduzierte Wälzkontaktermüdung," *Fraunhofer Verlag*, Freiburg, 2015.
- [34] K. L. Johnson, *Contact Mechanics*, Cambridge: Cambridge University Press, 1987.
- [35] T. Fett and D. Munz, "Fracture Mechanics," in *Handbook of Advanced Ceramics*, vol. 1, S. Somiya, F. Aldinger, C. Nils, R. Spriggs, K. Uchino, K. Koumoto and M. Kaneno, Eds., Amsterdam, Elsevier, 2003, pp. 647-706.
- [36] G. Glinka and G. Shen, "Universal features of weight functions for cracks in mode I.," *Engineering Fracture Mechanics*, pp. 1135-1146, 1991.
- [37] G. Sha and C.-T. Yang, "Weight functions of radial cracks emanating from a circular hole in a plate," in *Fracture Mechanics: Seventeenth Volume*, Albany, New York, 1986.
- [38] G. Sih, *Handbook of Stress Intensity Factors*, Pennsylvania: Lehigh University Bethlehem, 1973.
- [39] G. Glinka, "Development of weight functions and computer integration procedures for calculating stress intensity factors around cracks subjected to complex stress fields," *Stress and Fatigue-Fracture Design SaFFD, Inc.*, Ontario, Canada, 1996.

- [40] A. Kiciak, G. Glinka and D. J. Burns, "Calculation of stress intensity factors and crack opening displacements for cracks subjected to complex stress fields," *Journal of Pressure Vessel Technology*, vol. 125, no. 3, pp. 260-266, 2003.
- [41] R. Raga, I. Khader, Z. Chlup and A. Kailer, "Damage initiation and evolution in silicon nitride under non-conforming lubricated hybrid rolling contact," *Wear*, Vols. 360-361, p. 147–159, 2016.
- [42] R. Danzer, "Ceramics: Mechanical performance and lifetime prediction," in *The Encyclopedia of Advanced Materials*, D. Bloor, R. J. Brook, M. C. Flemings, S. Mahajan and R. W. Cahn, Eds., Pergamon, 1994, p. 385–398.
- [43] M. Herrmann, I. Schulz, A. Bales, K. Sempf and S. Hoehn, " "Snow flake" structures in silicon nitride ceramics – Reasons for large scale optical inhomogeneities," *Journal of the European Ceramic Society*, vol. 28, no. 5, pp. 1049-1056, 2008.
- [44] X. Wang and S. Lambert, "Stress intensity factors for low aspect ratio semi-elliptical surface cracks in finite-thickness plates subjected to nonuniform stresses.," *Engineering Fracture Mechanics*, vol. 51, no. 4, pp. 517-537, 1995.